# Ultra-Wide-Band Traveling-Wave Photodetectors for Photonic Local Oscillators

Andreas Stöhr, *Member, IEEE*, Andrei Malcoci, Andres Sauerwald, Iván Cámara Mayorga, Rolf Güsten, and Dieter Stefan Jäger, *Fellow, IEEE*

*Invited Paper*

***Abstract*—This paper reviews recent advances in the development of high-speed 1.55-$\mu$m traveling-wave p-i-n photodetectors (TWPD) for photonic millimeter-wave and submillimeter-wave local oscillators. We first discuss the basic physics and performances of high-speed 1.55-$\mu$m TWPD. Next, we present a frequency-domain optical-heterodyne measurement technique for ultra-wide-band characterization of the TWPD and photonic transmitter modules within the frequency range from almost dc up to more than 1 THz. We further demonstrate ultra-wide-band (0.02–0.7 THz) photonic transmitter modules consisting of a high-speed TWPD coupled to a broad-band bow-tie antenna as well as a narrow-band 0.46-THz photonic transmitter module producing output power levels sufficient to operate a superconductor–insulator–superconductor (SIS) astronomical receiver under optimum conditions. Finally, we will report on ultra-wide-band (0.06–1 THz) photonic transmitter modules consisting of high-speed TWPDs coupled to various rectangular metallic waveguides (WR10, WR8, and WR5).**

***Index Terms*—Microwave photonics, millimeter-wave (mm-wave) generation, optical heterodyne, p-i-n photodiodes, photodetector, terahertz (THz) generation.**

## I. Introduction

MILLIMETER WAVES (mm waves) and submillimeter waves (submm waves) are currently attracting a great deal of interest in radio astronomy, antenna remoting, imaging, and broad-band wireless communications. A key challenge in that regard is the development of ultra-wide-band and tunable local oscillators (LOs) in these wavelength ranges. Purely electrical LO sources consisting of a Gunn diode and a subsequent multiplier chain suffer from their poor frequency coverage and limited tuneability. To overcome these technological limitations of all-electronic LOs, there has been increasing interest in developing a photonic LO (PLO) capable of operating up to submm-wave frequencies [2]–[11]. Generally, in a PLO a (sub)mm-wave signal is generated by square-law detection of a highly stable phase-locked optical heterodyne signal employing an ultrafast photodiode (PD) [1]. Since the frequency of the generated (sub)mm-wave signal depends on the beat-frequency difference between the two optical carriers of the heterodyne signal, it can be easily tuned over a ultra-wide range by varying the frequency of one optical carrier. In addition to the ultra-wide-band capabilities, PLOs offer further advantages in terms of power dissipation, source size, and remote tuneability.

The work presented here is motivated by fabricating prototype PLO sources for the Atacama large-millimeter array (ALMA) telescope array [12]. ALMA requires frequency-stable, low-phase-noise local oscillators with a tuneability from 0.03–0.95 THz and some microwatts of output power at each of the 64 antenna sites for the remote down-conversion of the received astronomical radio signals. Since the distance between the central location and the various antennas that make up the array can extend to 10 km and more, the usage of PLO operating in the optical $C$ band is preferable due to low fiber attenuation and the availability of high-power erbium-doped fiber amplifiers (EDFAs) in that band. As illustrated in Fig. 1, a PLO mainly consists of a highly stable optical source and a high-speed PD in the remote photonic (sub)mm-wave transmitter.

This paper focuses on recent achievements in high-speed 1.55-$\mu$m traveling-wave photodetectors (TWPDs) and practical developments of ultra-wide-band (sub)mm-wave transmitter modules. Results on the recent developments in highly stable phase-locked optical sources can be found in [12]–[14]. At first, the basic physics technologies and performances of high-speed 1.55-$\mu$m TWPD are theoretically and experimentally investigated. This is followed by a description of a frequency-domain optical heterodyne measurement setup for characterizing photonic (sub)mm-wave transmitter modules from almost dc up to more than 1 THz. In Sections IV and V, photonic transmitter modules are presented yielding either quasi-optical free-space radiation of the generated (sub)mm-wave signals or guided transmission within a rectangular metallic waveguide. In detail, ultra-wide-band (0.02–0.7 THz) bow-tie-antenna-integrated and narrow-band 0.46-THz slot-antenna-integrated TWPD will be presented as well as rectangular-waveguide-coupled TWPD that enable (sub)mm-wave generation from 0.06 to 1 THz.

Manuscript received June 24, 2003; revised September 19, 2003. The design and fabrication of the photonic terahertz transmitter was funded in part by the European Southern Observatory (ESO) under Contract 59608/MAP/00/6750/RFI.

A. Stöhr, A. Malcoci, A. Sauerwald, and D. S. Jäger are with ZHO/Optoelektronik, Universität Duisburg-Essen (formerly Gerhard-Mercator Universität Duisburg), 47057 Duisburg, Germany.

I. C. Mayorga and R. Güsten are with Max Planck-Institut für Radioastronomie, 53121 Bonn, Germany.

Digital Object Identifier 10.1109/JLT.2003.822257

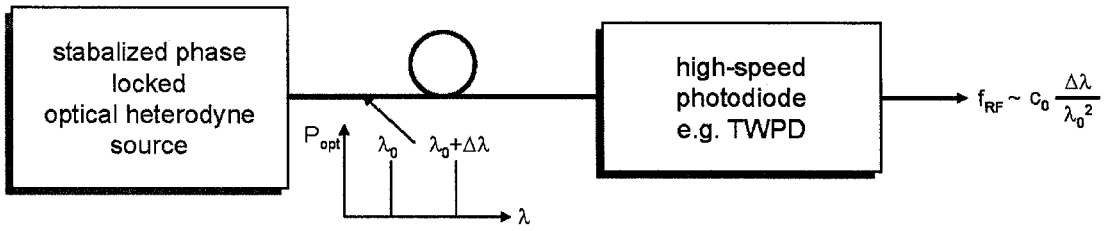


Fig. 1. Schematic of optical heterodyne signal generation in an photonic local oscillator (PLO).

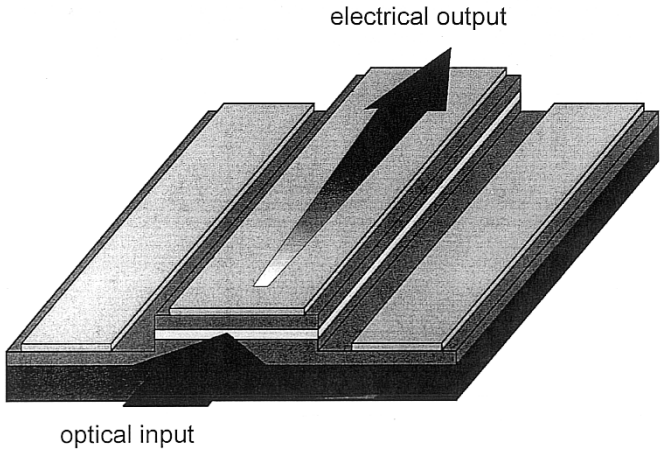


Fig. 2. Concept of a TWPD with an optical rib waveguide and a coplanar transmission line.

## II. High-Speed 1.55-$\mu$m TWPDs

A sketch of the high-speed 1.55-$\mu$m TWPD investigated in this paper is shown in Fig. 2. The detector consists of an optical waveguide and an electrical transmission line. The optical heterodyne signal launched into the optical-strip-loaded waveguide is gradually absorbed, resulting in a distributed current generation along the detector's length that contributes to the overall current propagating along the electrical transmission line of the TWPD. The TWPD differs from a lumped element in a non-radiatevely coupled (RC) time-limited response exhibiting superior high-frequency performances which has recently been theoretically and experimentally investigated [15]–[20].

The waveguide structure of the TWPDs investigated in this work was grown on an InP:Fe substrate by metal organic vapor phase epitaxy (MOVPE). The optical core is embedded in the intrinsic region of a p-i-n diode. The absorptive nonintentionally doped (intrinsic) 100-nm-thick InGaAs ($W_g = 0.75$ eV) layer is located on top of a slightly n-doped ($1.10^{18}$ cm$^{-3}$) 900-nm-thick InGaAsP ($W_g = 0.944$ eV) core. The P-doped ($2.10^{18} - 1.10^{19}$ cm$^{-3}$) 600-nm-thick top cladding layer is built of InAlAs ($W_g = 1.46$ eV), and the bottom cladding layer below the optical core consists of an N-doped ($1.10^{18}$ cm$^{-3}$) 600-nm-thick InP ($W_g$ =1.33 eV) layer. On top of the upper P-doped cladding, a 50-nm-thin p-doped ($1.10^{19}$ cm$^{-3}$) lattice-matched InGaAs ($W_g = 0.75$ eV) contact layer finalizes the structure. The technological realization of the optical-strip-loaded waveguide, together with the fabrication process of the hybrid electrical microstrip/coplanar transmission line, consists of a self-aligned etching process and two metallization steps for the p- and n-type ohmic contacts. At first, e-beam evaporation of the p-type Ti–Pt–Au (30/20/300-nm) center contact is performed, which is also used as a mask for the subsequent etching processes of the optical waveguide. Selective wet-chemical etching of the contact layer, the top cladding, and the absorptive InGaAs core layer is performed followed by the Ge–Pt–Au (30/30/300-nm) metallization to form the n-type ground contact of the electrical transmission line.

For studying the physical effects limiting the frequency response of a TWPD and to investigate the impact of design variations on the detector's performance, a theoretical analysis has been developed. It includes the relevant physical phenomena associated with the vertical transport of the photo-generated carriers as well as the longitudinal optical and electrical wave propagation within the TWPD [19]. As can be seen in Fig. 3, the model is based on a quasi-static equivalent transmission line circuit, including a distributed current source $i'$ that accurately describes the dynamics of the vertical transport of the photo-generated carriers at any point along the detector. This current source includes the intrinsic effects, such as the transit time limitation due to the propagation through the intrinsic layers. By neglecting transversal and longitudinal carrier transport and assuming harmonic time dependence, the distributed current source $i'$ is found from one-dimensional complex continuity equations for the electron and hole densities $n(x)$ and $p(x)$ to be

$$i'(z) = \frac{w}{d_0} \cdot \frac{q \cdot G_0 \cdot \exp\left(-\gamma_{\text{opt}} \cdot z\right)}{j\omega} \cdot \left[ \begin{array}{l} v_n \cdot \left( \frac{v_n}{j\omega} - d_0 - \frac{v_n}{j\omega} \cdot \exp\left(-j\omega \cdot \frac{d_0}{v_n}\right)\right) \\ +v_p \cdot \left( \frac{v_p}{j\omega} - d_0 - \frac{v_p}{j\omega} \cdot \exp\left(-j\omega \cdot \frac{d_0}{v_p}\right)\right) \end{array} \right]. \quad (1)$$

Here, $w$ and $d_0$ denote the optical waveguide width and the thickness of the nonintentionally doped absorbing layer, respectively. Further $v_n$ and $v_p$ describe the drift velocities of electron and holes. $G_0$ is the carrier generation rate and $\gamma_{\text{opt}}$ is the optical wave propagation constant [19]. Next, the integrated contribution of the distributed current source $i'$ to the overall electrical wave propagating along the slow-wave transmission line [21] of the TWPD is calculated using a quasi-transmission electron microscopy analysis in conjunction with the quasi-static equivalent circuit model shown in Fig. 3(a). Here, the photo-generated current source per unit length is represented by $i'(z)$. $R'$ and $L'$ are the resistance and the inductance of the metal center conductor per unit length, respectively. $R'_s$ represents the semiconductor losses associated with transverse current flow in the doped core

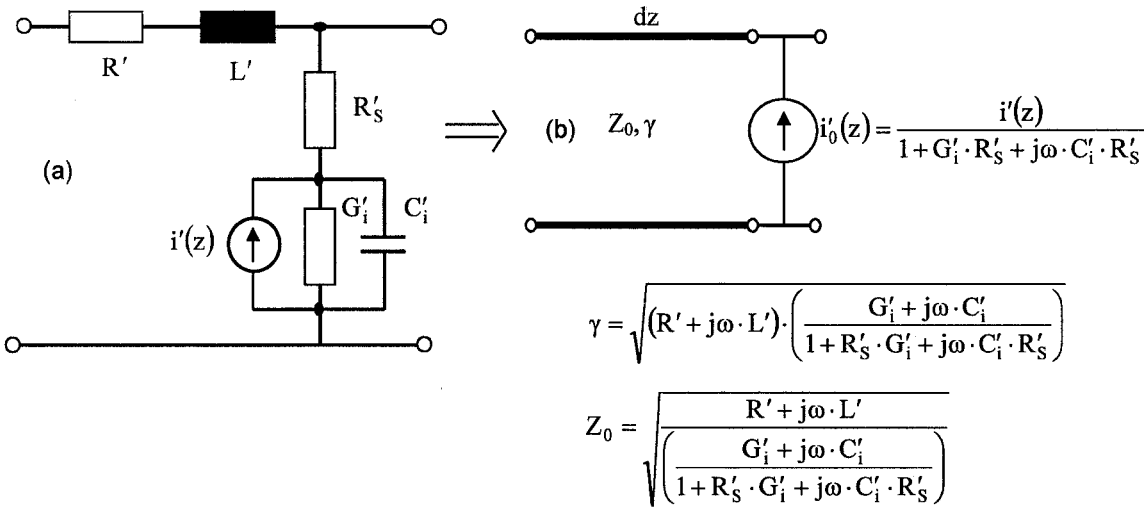


Fig. 3. (a) Quasi-static equivalent transmission line circuit model of the TWPD (b) transferred into a passive transmission line circuit loaded with a current source $i'_0$. The dependence of the characteristic impedance $Z_0$, the propagation constant $\gamma$, and the current source $i'_0$ on the TWPD circuit elements are given.

and cladding layers and $C'_{\rm i}$ and $G'_{\rm i}$ are the capacitance and the conductance of the intrinsic core layer per unit length. The air capacitance, which is typically very small in value, is neglected. By transforming the current source $i'(z)$, we can convert the equivalent transmission line circuit into a form where the active current source is in parallel to a completely passive electrical transmission line represented by its characteristic impedance $Z_0$ and propagation constant $\gamma$ [Fig. 3(b)]. Based on the transmission line model (TLM), the radio frequency output power $P_{\rm out,el}$ delivered to the load impedance $Z_L$ is analytically determined to be (2), shown at the bottom of the page, with

$$r_e = \frac{Z_E - Z_0}{Z_E + Z_0} \tag{3}$$

and

$$r_a = \frac{Z_L - Z_0}{Z_L + Z_0} \tag{4}$$

representing the reflection coefficients at the input and output ports of the TWPD, respectively.

In order to quantitatively simulate the generated power delivered to a load impedance $Z_L$, the circuit parameters of the TWPD equivalent circuit need to be determined. Generally, these parameters are frequency dependent, but for frequencies in excess of 20 GHz, the parameters $L'$, $R'_{\rm s}$, $C'_{\rm i}$, and $G'_{\rm i}$ are considered to be constant. Only $R'$ increases with the square root of frequency due to the skin effect. In good approximation, $C'_{\rm i}$ can be determined by $C'_{\rm i} = \varepsilon_0\varepsilon_\rho \cdot w/d_0$, resulting in 7.995 pF/mm for the investigated TWPD structure with an intrinsic region of $d_0 = 100$ nm and a width of $w = 6$ $\mu$m. The

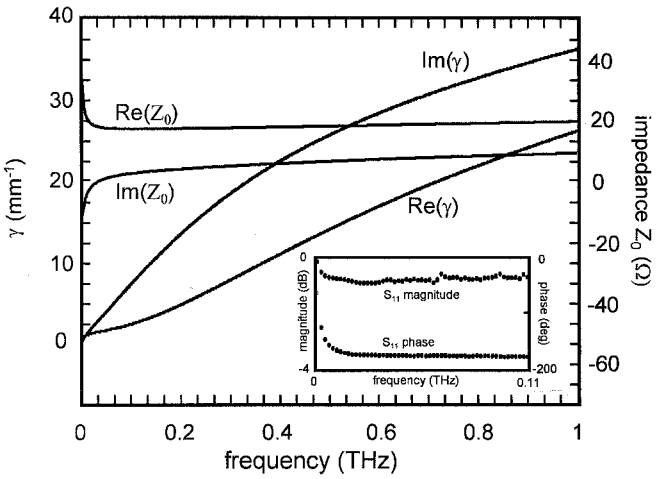


Fig. 4. Calculated frequency dependence of the characteristic impedance and electrical propagation constant of a 50-$\mu$m-long and 6-$\mu$m-wide TWPD. The inset shows the measured $S_{11}$ parameter of the same device up to 110 GHz.

constant conductor resistance per unit length at frequencies below 10 GHz is given by $R' = \rho_{\rm Au}/(w \cdot d_{\rm met})$, resulting in 18.5 $\Omega$/mm. The series resistance mainly due to the carrier transport in the doped semiconductor layers is approximately $R'_{\rm s} \sim 0.25\ \Omega \cdot$ mm for a 6-$\mu$m-wide center contact with a 15-$\mu$m separation between the center and the ground electrode. The parallel conductance $G'_{\rm i} \sim 10$ mS/mm and the transversal inductance $L' \sim 0.08$ nH/mm were experimentally determined from S-parameter measurements performed up to 110 GHz (inset in Fig. 4). With all the equivalent circuit parameters known, the complex characteristic impedance $Z_0$ and the

$$P_{\rm out,el} = \frac{i_0'^2 \cdot Z_L}{8} \cdot \left[ \begin{array}{l} \frac{1}{\gamma_{\rm el} - \gamma_{\rm opt}} \cdot \left(\exp\left(-\gamma_{\rm opt} \cdot l\right) - \exp\left(-\gamma_{\rm el} \cdot l\right)\right) \\ -\frac{r_a}{(1 - r_a \cdot r_e \cdot \exp(-2 \cdot \gamma_{\rm el} \cdot l)) \cdot (3 \cdot \gamma_{\rm el} - \gamma_{\rm opt})} \cdot \left(\exp\left(-\gamma_{\rm opt} \cdot l\right) - \exp\left(-3 \cdot \gamma_{\rm el} \cdot l\right)\right) \\ -\frac{r_e}{(1 - r_a \cdot r_e \cdot \exp(-2 \cdot \gamma_{\rm el} \cdot l)) \cdot (\gamma_{\rm el} + \gamma_{\rm opt})} \cdot \left(\exp\left(-\gamma_{\rm opt} \cdot l - 2 \cdot \gamma_{\rm el} \cdot l\right) - \exp\left(-\gamma_{\rm el} \cdot l\right)\right) \end{array} \right]^2 \tag{2}$$

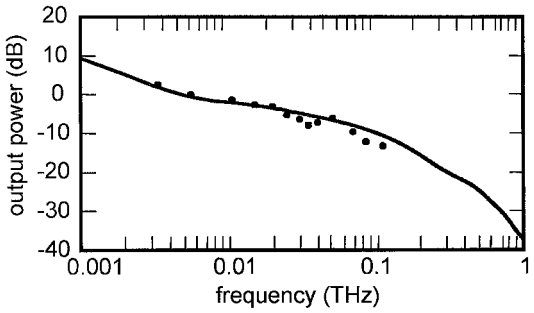


Fig. 5. Simulated frequency response of a 50-$\mu$m-long and 6-$\mu$m-wide TWPD. Dots indicate measured output power levels of the same device up to 110 GHz.

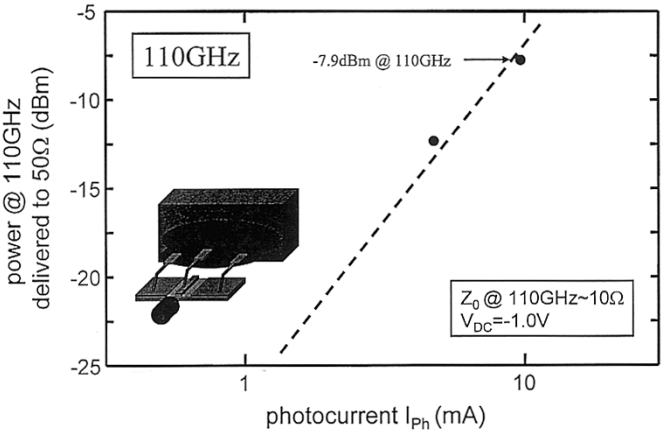


Fig. 6. On-wafer measured output power at 110 GHz delivered by the TWPD to a 50-$\Omega$ load impedance with respect to the detector's photocurrent.

complex electrical propagation constant $\gamma$ of the TWPD transmission line are calculated. In Fig. 4, the theoretically determined characteristic impedance and propagation constant of a 50-$\mu$m-long and 6-$\mu$m-wide TWPD are plotted up to 1-THz submm-wave frequency. The inset in Fig. 4 shows the $S_{11}$ parameter of the same device measured up to 110 GHz. As can be seen from Fig. 4, the characteristic impedance of the investigated TWPD is quite constant within the frequency range from 20 GHz to 1 THz, with an absolute value varying between 15 and 20 $\Omega$.

In Fig. 5 the power delivered by the TWPD to a load impedance of $Z_L = 50\ \Omega$ is calculated using (1)–(4) for frequencies up to 1 THz. In addition, the theoretical result is compared in Fig. 5 with experimental data of the investigated device up to 110 GHz. For measuring the power delivered by the TWPD to a 50-$\Omega$ impedance, an on-wafer 1.5- $\mu$m optical heterodyne setup with external mixers (50–110 GHz) was used [4]. As can be seen, there is good agreement between the measured and the simulated data with a maximum variation of approximately 3 dB. This proves the accuracy and reliability of the analytical model. The total roll-off of 50 dB for a the full frequency span from dc to 1 THz is due to the transit time effects and intrinsic effects arising from carrier transport in the doped sections of the TWPD. In addition, propagation effects, such as microwave losses and velocity mismatch, contribute to the total roll-off. At frequencies in excess of 0.1 THz, we found that the delivered power decreases with the frequency by about $f^{-3}$ for the investigated devices. Quantitatively, the power delivered to 50 $\Omega$ at 110 GHz was measured in dependence of the photocurrent of the TWPD. The dc responsivity of the 50-$\mu$m-long and 6-$\mu$m-wide TWPD was 0.08 A/W without an antireflection coating at the front facet. As can be seen from Fig. 6, the maximum power level achieved is $-7.9$ dBm at a photocurrent of $I_{\rm ph} = 10$ mA. Due to the mismatch between the characteristic impedance of the investigated TWPD and the 50-$\Omega$ load, we estimate the generated power level to be about 8 dB larger. Thus, the maximum available power level at 110 GHz is expected to be about 1 mW at a photocurrent of 10 mA. As can be further seen from Fig. 6, no power saturation is observed at photocurrent levels of 10 mA; thus, we expect higher power levels at larger photocurrents. Currently, the maximum safe photocurrent of the fabricated TWPD is typically about 20 mA. In order to further increase the generated power levels at (sub)mm-wave frequencies, one must further suppress saturation effects due to the high photocurrent in the TWPD but also to reduce penalties arising from transit time and wave propagation effects.

## III. Optical Heterodyne (Sub)mm-Wave Measurement Setup

To experimentally investigate the frequency response of the TWPD and to measure the output power levels of a packaged photonic transmitter, we use an optical heterodyne setup with two free-running diode lasers to generate an optical heterodyne signal with the desired beat frequency in the (sub)mm-wave regime. For frequencies up to 220 GHz, we employ external single-diode harmonic mixers and commercial coplanar microprobes for performing on-wafer measurements of the TWPD [4]. This setup typically exhibits an equivalent noise level of less than $-50$ dBm @ 200 GHz using a 10-kHz resolution bandwidth. The low dynamic range of the setup is significantly limited by the jitter produced by the free-running optical heterodyne source. In terms of maximum frequency, the setup is currently limited to the mm-wave region since there are no commercial external mixers and coplanar on-wafer probes available for submm-wave frequencies. Therefore, to investigate the performance of the TWPDs and of the packaged transmitters at higher frequencies up to 1 THz, either a liquid helium cooled bolometer with a typical noise equivalent power (NEP) of about 2 pW/Hz$^{-1/2}$, or a Golay cell with a typical NEP of 100–200 pW/Hz$^{-1/2}$ can be used. Although the Golay cell does not provide such a good NEP, it does not require any expenditure for liquid helium cooling, since it operates at room temperature. Therefore, it is well suited for fast characterization of the photonic transmitters. The schematic of the optical heterodyne setup employing the Golay cell is shown in Fig. 7. The linearly polarized optical output signals of two free-running external-cavity laser diodes are combined using a 3-dB optical coupler. The polarization state of both lasers is adjusted to each other by tuning the polarization state of the tuned laser using a polarization controller. The combined optical heterodyne signal is amplified by a high-power EDFA. A variable optical attenuator is employed for performing power-dependent measurements.

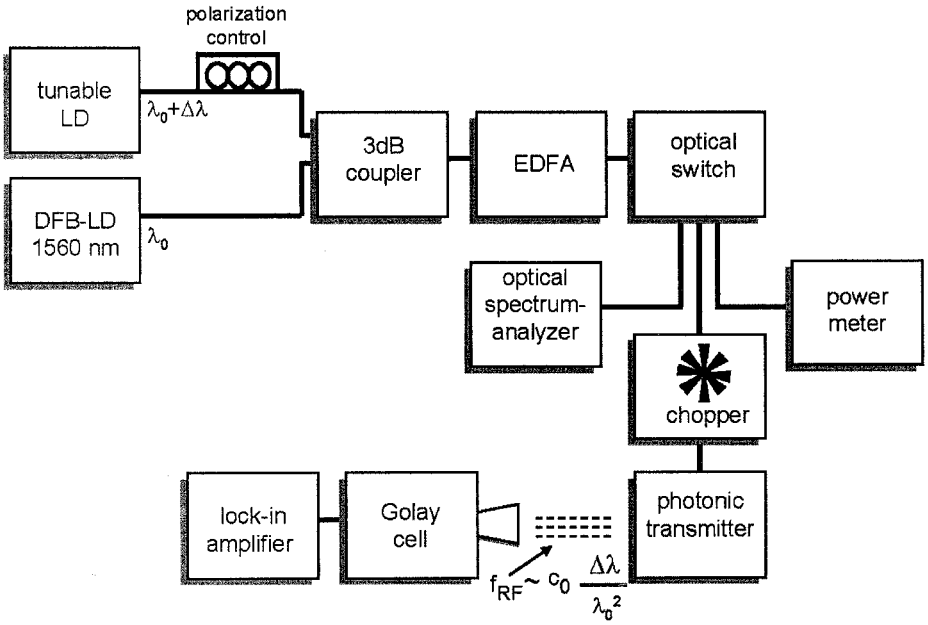


Fig. 7. Optical heterodyne measurement setup with a Golay cell for ultra-wide-band (almost dc to 1 THz) characterization of the TWPD and the photonic transmitter.

Optical input power to the TWPD is monitored by an optical power meter, and an optical spectrum analyzer is used to measure the beat frequency. The TWPDs are reverse-biased using a dc voltage source with internal current monitoring. The generated (sub)mm-wave power is radiated directly into the Golay cell without using any quasi-optical lenses between the photonic transmitter and the Golay cell. Since the Golay cell function relies on a thermal effect, it requires a low-frequency modulated input signal. To achieve this, we either modulate (20 Hz) the optical heterodyne signal using a chopper, or the dc bias supplied to the TWPD, or both.

## IV. Photonic Terahertz Transmitter Employing Antenna-Integrated 1.55-$\mu$m TWPD

To investigate the capabilities of a photonic LO to pump the SIS junction of an astronomical receiver, we have fabricated a photonic 0.46-THz transmitter. A sketch of the photonic transmitter chip used for this experiment is shown in Fig. 8(a). Here, the TWPD was monolithically integrated with a planar full-wave slot antenna resonant at 460 GHz. Furthermore, a passive bias-T was integrated employing radial stubs as low-pass filters. The scanning electron microscope (SEM) pictures in Fig. 8(b) and (c) show top views of an array of 0.46-THz and 0.65-THz transmitter chips and a single cleaved 0.46-THz transmitter chip, respectively. The inset in Fig. 8(c) shows an enlarged SEM picture of the active TWPD, the planar slot antenna, and the low-pass radial stubs and bias feed line. The overall dimensions of a single transmitter chip is $2266 \times 1700$ $\mu$m$^2$, and a total number of about 300 transmitters is fabricated on a single 2" InP substrate. Next, the transmitter chip was mounted on a hemispherical silicon lens with a diameter of 10 mm, as shown in Fig. 8(d). The silicon lens couples the antenna to free space, producing a near-Gaussian submm-wave beam that can be re-imaged on any receiver optics (lens and horn). Finally, the lens with the transmitter chip was packaged, as can be seen from Fig. 8(e) and (f).

To investigate the capabilities of the packaged transmitter module, an astronomical receiver with an SIS junction for down-converting the received signals was employed. During the experiment, all receiver components are at liquid helium temperature. We first used a 460-GHz solid-state oscillator chain consisting of a Gunn oscillator with a subsequent tripler to pump the SIS junction of the receiver. The output power of the solid-state oscillator was adjusted for optimum sensitivity (i.e., lowest noise temperature) of the SIS junction, and the corresponding dc-bias curve of the SIS junction was recorded (black line in Fig. 9). Hereafter, the solid-state oscillator signal was replaced by the optically generated LO signal from the transmitter module. Different dc-bias curves of the SIS junction were recorded as a function of laser input power level, i.e., as a function of the detector's photocurrent (gray lines in Fig. 9). The inset in Fig. 9 shows a photo of the employed liquid helium cooled receiver. As can be seen from Fig. 9, at a photocurrent of about 20 mA, the power generated by the PLO is equivalent to the power generated by the solid- state LO. Thus, the developed photonic transmitter is capable of pumping the SIS junction of the receiver under optimum conditions. In Fig. 10, the total submm-wave power generated by the transmitter module is shown as a function of the photocurrent in the TWPD. As can be seen, the power levels follow the square-law principle; no saturation effects are observed for photocurrents up to 20 mA.

Although resonant-type antennas exhibit a sufficiently large bandwidth to cover a single astronomical band [12], it is of great interest to develop an ultra-wide-band photonic transmitter that could eventually be employed not just for a single band but for a number of astronomical bands. To achieve such an ultra-wide-band photonic (sub)mm-wave generation, we have integrated a high-speed TWPD with a planar bow-tie antenna which offers a reasonable constant impedance that can be matched to

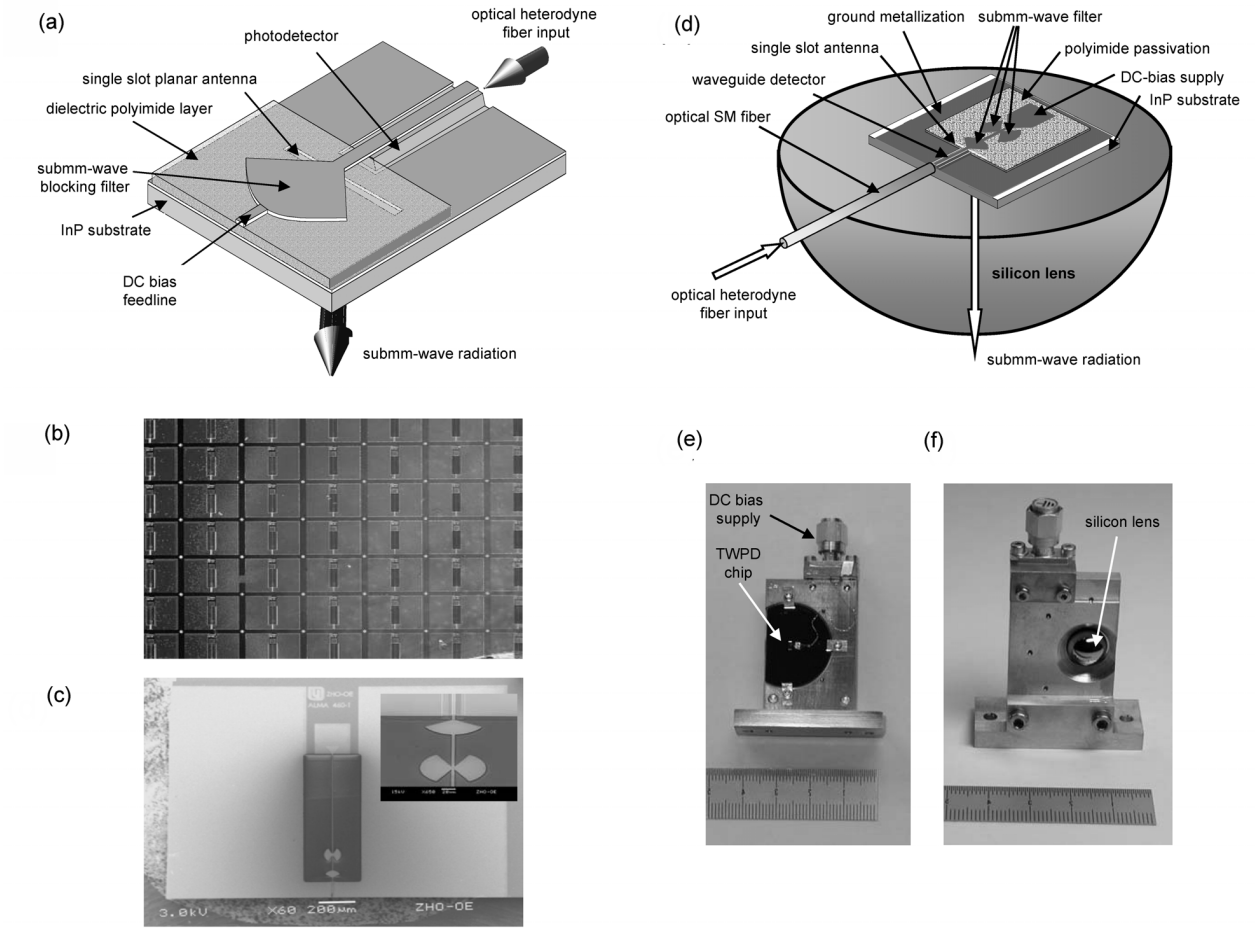


Fig. 8. (a) Schematic of a photonic 0.46-THz transmitter consisting of a TWPD monolithically integrated with a planar full-wave single slot antenna and submm-wave filter structures to enable the dc-bias supply for the detector. SEM pictures of (b) fabricated 0.46-THz and 0.65-THz photonic transmitter array and of (c) a single cleaved 0.46-THz chip. (d) Schematic of a photonic transmitter chip mounted on a hemispherical silicon lends as well as (e), (f) photos of the packaged photonic transmitter module.

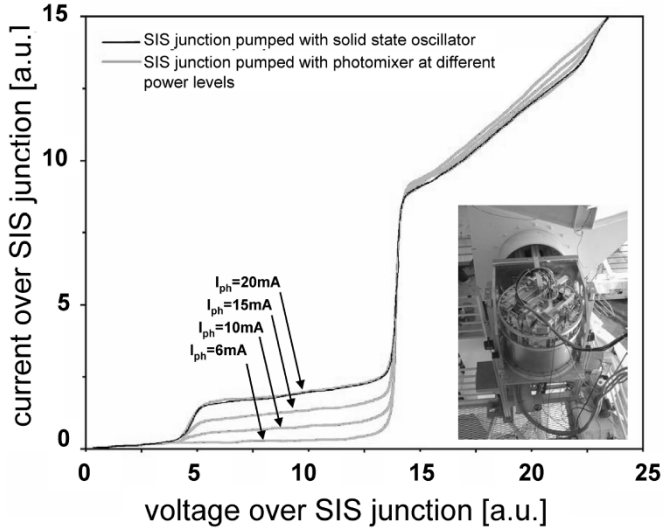


Fig. 9. dc current-voltage curves of the SIS junction of a 460-GHz astronomical receiver (photo) pumped by a Gunn oscillator (black line) or by the photonic 0.46-THz transmitter [Fig. 8(e) and (f)] at different photocurrent levels.

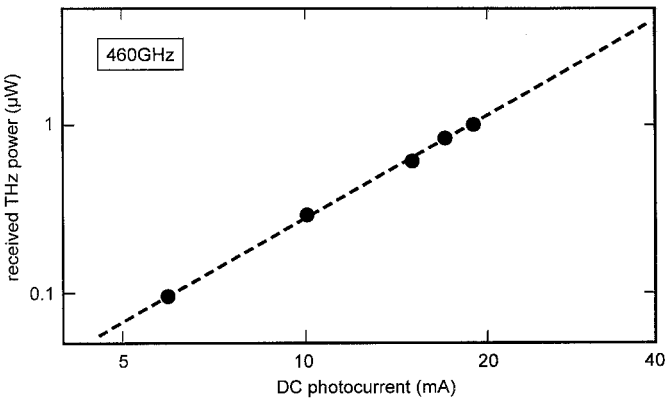


Fig. 10. Generated 0.46-THz submm-wave power with respect to the photocurrent in the TWPD.

the detector's impedance within a very large frequency span. A schematic of the bow-tie-antenna-integrated TWPD is shown in Fig. 11. The inset shows a photograph of a fabricated chip. The length and width of the TWPD and the opening angle of the bow-tie antenna are 116 $\mu$m, 3.2 $\mu$m, and $\theta = 9.4^{\circ}$, respectively. The chip was also mounted on a hemispherical silicon lens and packaged as described together with Fig. 8(e) and (f). The packaged module was investigated using the experimental

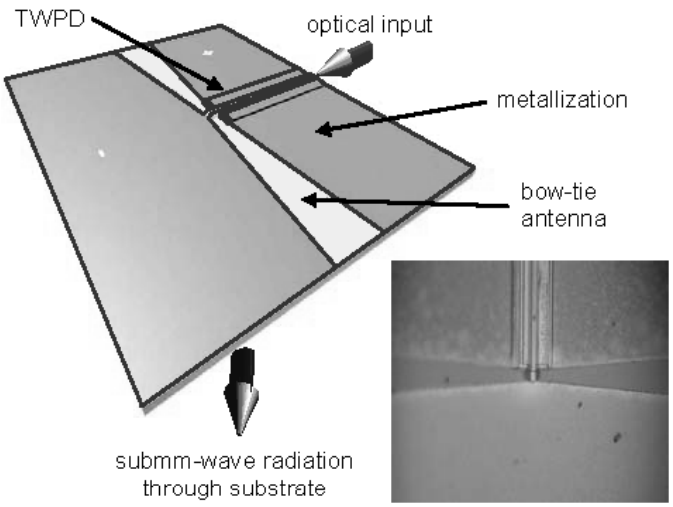


Fig. 11. Schematic of a TWPD monolithically integrated with a planar ultra-wide-band bow-tie antenna. The inset shows an SEM picture of a fabricated transmitter chip.

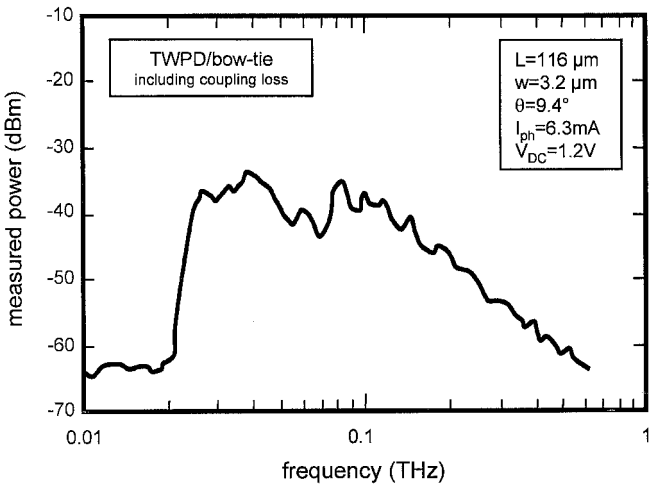


Fig. 12. Ultra-wide-band (sub)mm-wave power generation employing a bow-tie-antenna-integrated TWPD.

setup shown in Fig. 7. Here, the generated power was quasi-optically radiated into the Golay cell without using any imaging optics. Fig. 12 shows the measured (sub)mm-wave power received by the Golay cell. Coupling losses associated with the quasi-optical radiation into the Golay cell have not been excluded from the measured results. As can be seen from Fig. 12, the maximum power received by the Golay cell is about half a microwatt for a photocurrent of approximately 6 mA. The generated power level is fairly flat within a frequency range of 20 GHz to 0.1 THz. Above 0.1 THz, we observed that the power level approximately decreases with frequency to a power of 3, which is in accordance to the simulations presented in Fig. 5. Similar frequency dependence of wide-band-antenna-integrated PD was also found in [7]. Although the power levels that have currently been achieved employing wide-band-antenna-integrated PDs is not quite large enough for pumping astronomical receivers at terahertz frequencies, the approach offers promising

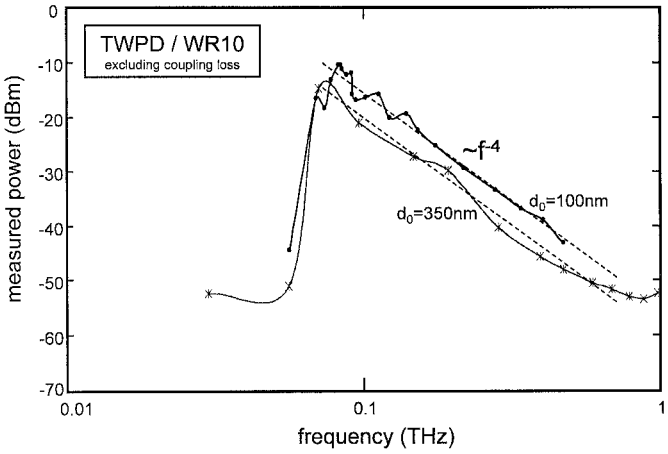


Fig. 13. Ultra-wide-band (sub)mm-wave power generation employing rectangular-waveguide (WR10)-coupled TWPDs with different intrinsic region thicknesses of 100 and 350 nm.

perspectives for wide-band photonic LO at least up to some 100 GHz, provided that high-photocurrent diodes [22]–[24] with improved high-frequency performance are employed. However, at very high frequencies, approximately 1-THz narrow-band antennas might be more favorable since they usually offer higher efficiency and can be more easily matched to the detector's impedance.

## V. Photonic Terahertz Transmitter Employing Waveguide-Coupled 1.55-$\mu$m TWPD

Although most photonic LOs utilize the free-space radiation of the generated (sub)mm-wave power, there are specific applications where guided transmission in a rectangular waveguide is more desirable. Efficient optical heterodyne generation of guided (sub)mm waves has already been demonstrated in [9]–[11] up to about 600 GHz using WR10 waveguide-integrated high-speed PDs. Here, we will demonstrate ultra-wide-band guided transmission up to 1 THz employing high-speed TWPD coupled to different rectangular waveguides (WR10, WR8, and WR5). For experimental characterization, we utilize fabricated TWPD and commercial on-wafer coplanar to waveguide transitions. The devices are characterized using the setup described in Fig. 7 by quasi-optical coupling the power from the waveguide into the Golay cell. The coupling loss is calibrated using a $w$-band mm-wave module. In Fig. 13, ultra-wide-band (sub)mm-wave generation is demonstrated up to 1 THz using different TWPD coupled to WR10 waveguides. As can be seen, the maximum power level of about 100 $\mu$w is achieved at frequencies slightly below 0.1 THz within the $W$ band. Here, the TWPD with an intrinsic region thickness of $d_0 = 100$ nm generates about 5 dB more power, which is traced back to a lower transit time penalty. It can be further observed from Fig. 13 that the power decreases with frequency to the power of 4, which is a somewhat higher decrease as compared with the antenna-integrated transmitter. Similar results were also found in [9] and [10]. To further investigate the power dependence on frequency, the TWPDs were coupled to smaller waveguides (WR8 and WR5) since those waveguides exhibit significantly less modes that can propagate at frequencies

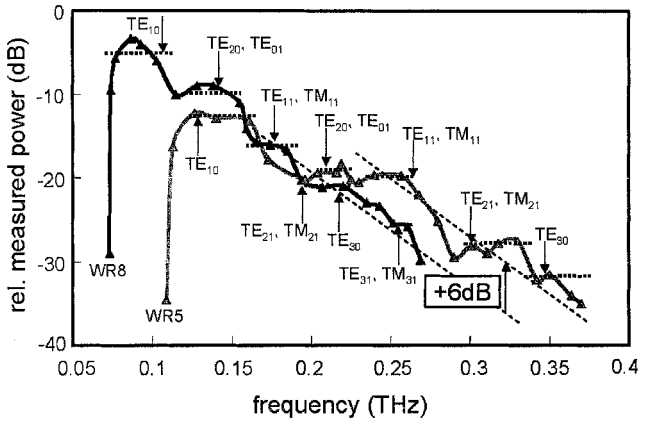


Fig. 14. Ultra-wide-band (sub)mm-wave power generation employing a WR8 and a WR5 rectangular-waveguide-coupled TWPD.

above 100 GHz. Fig. 14 shows the generated power level using the same TWPD coupled to a WR8 and a WR5 waveguide. In addition, the cutoff frequencies of the higher order modes that can propagate in the two waveguides are indicated by arrows in Fig. 14. A step-like response is observed with an almost flat response around the cutoff frequencies of the higher order modes. At lower frequencies, the TWPD generates higher power levels when coupled to a WR8 waveguide, but at frequencies above 220 GHz, the power level is about four times larger when the TWPD is coupled to a WR5 waveguide.

## VI. Conclusion

In conclusion, we have presented a thorough theoretical and experimental investigation of photonic LO (PLO) signal generation employing high-speed TWPDs. Theoretically, we studied the high-frequency performance of TWPD up to 1 THz using an equivalent circuit and a transmission line model for the TWPD. The accuracy of the theoretically predicted results has been confirmed up to a 110-GHz mm-wave frequency. We demonstrated a narrow-band 0.46-THz packaged photonic transmitter module that is capable of pumping the SIS junction of an astronomical receiver under optimum conditions. We further demonstrated an ultra-wide-band (0.02–0.7 THz) photonic transmitter utilizing a bow-tie-antenna-integrated TWPD, as well as an ultra-wide-band (0.06–1 THz) photonic transmitter utilizing a WR10 waveguide-coupled TWPD.

## Acknowledgment

The authors would like to thank F. Siebe, F. Schäfer and P. van der Waal from the Max-Planck Institut für Radioastronomie, Bonn, Germany, for their collaboration during the characterization of the integrated photonic transmitters as well as for the design of the resonant slot line antennas and their corresponding microstrip circuitry. The authors are further thankful to Anritsu Deutschland GmbH and Anritsu France SA for supporting a 110 GHz NWA. Finally, the authors wish to thank K. Lill and I. Schestakov from Universität Duisburg-Essen for the fabrication of the transmitter chips in the clean-room facilities of the ZHO.

## References

[1] J. Soohoo, S.-K. Yao, J. E. Miller, R. R. Shurtz II, Y. Taur, and R. A. Gudmundsen, "A laser-induced traveling-wave device for generating millimeter-waves," *IEEE Trans. Microwave Theory Tech.*, vol. 29, pp. 1174–1182, Nov. 1981.

[2] T. Nagatsuma, A. Hirata, Y. Royter, M. Shinagawa, T. Furuta, T. Ishibashi, and H. Ito, "A 120 GHz integrated photonic transmitter," in *Proc. Int. Topical Meeting Microwave Photonics MWP*, Oxford, U.K., Sept. 2000, pp. 225–228.

[3] T. Chau, N. Kaneda, T. Jung, A. Rollinger, S. Mathai, Y. Qian, T. Itoh, M. C. Wu, W. B. Shillue, and J. M. Payne, "Generation of millimeter waves by photomixing at 1.55 $\mu$m using InGaAs-InAlAs-InP velocity-matched distributed photodetectors," *IEEE Photon. Technol. Lett.*, vol. 12, pp. 1055–1057, Aug. 2000.

[4] A. Stöhr, R. Heinzelmann, C. Kaczmarek, and D. Jäger, "Ultra-broadband $\mathrm{K}_\alpha$ to W-band 1.55 $\mu$m travelling-wave photomixer," *Electron. Lett.*, vol. 36, no. 11, pp. 970–972, May 2000.

[5] A. Stöhr, R. Heinzelmann, K. Hagedorn, R. Güsten, F. Schäfer, H. Stüer, F. Siebe, P. van der Wal, V. Krozer, M. Feiginov, and D. Jäger, "Integrated 460 GHz photonic transmitter module," *Electron. Lett.*, vol. 37, pp. 1347–1348, Oct. 2001.

[6] A. Malcoci, A. Stöhr, K. Lill, F. Siebe, P. van der Wal, A. Sauerwald, R. Güsten, and D. Jäger, "Optical submillimeter-wave generation employing antenna integrated ultra-fast traveling-wave 1.55 $\mu$m photodetectros," in *IEEE MTT-S Int.*, Philadelphia, PA, June 2003, Paper TU6B-1.

[7] A. Hirata, T. Nagatsuma, R. Yano, H. Ito, T. Furuta, Y. Hirota, T. Ishibashi, H. Matsuo, A. Ueda, T. Noguchi, Y. Sekimoto, M. Ishiguro, and S. Matsuura, "Output power measurement of photonic millimeter-wave and sub-millimeter-wave emitter at 100–800 GHz," *Electron. Lett.*, vol. 38, no. 15, pp. 798–799, July 2002.

[8] H. Ito, T. Furuta, Y. Hirota, T. Ishibashi, A. Hirata, T. Nagatsuma, H. Matsuo, T. Noguchi, and M. Ishiguro, "Photonic millimeter-wave emission at 300 GHz using an antenna-integrated uni-traveling-carrier photodiode," *Electron. Lett.*, vol. 38, no. 17, pp. 989–990, Aug. 2003.

[9] P. G. Huggard, B. N. Ellision, P. Shen, N. J. Gomes, P. A. Davies, W. P. Shillue, A. Vaccari, and J. M. Payne, "Efficient generation of guided millimeter-wave power by photomixing," *IEEE Photon. Technol. Lett.*, vol. 14, pp. 197–199, Feb. 2002.

[10] ——, "Generation of millimeter and sub-millimeter waves by photomixing in a 1.55 $\mu$m wavelength photodiode," *Electon. Lett.*, vol. 38, no. 7, pp. 327–328, 2002.

[11] T. Noguchi, A. Ueda, H. Iwashita, S. Takano, Y. Sekimoto, M. Ishiguro, T. Ishibashi, H. Ito, and T. Nagatsuma, "Millimeter-wave generation using a uni-traveling-carrier photodiode," in *Proc. 12th Int. Symp. Space Terahertz Technology*, San Diego, CA, 2001.

[12] J. Payne, B. Shillue, and A. Vaccari, "Photonic techniques for use on the atacama large millimeter array," in *Proc. Int. Topical Meeting Microwave Photonics MWP*, Melbourne, Australia, Nov. 1999, pp. 105–108.

[13] P. Shen, P. A. Davis, W. P. Shillue, L. R. D'Addario, and J. M. Payne, "Millimeter-wave generation using an optical comb generator with phase-locked loops," in *Proc. Int. Topical Meeting Microwave Photonics*, Awaji, Japan, 2002, pp. 97–100.

[14] T. Yamamoto, H. Takara, and S. Kawanishi, "Generation and transmission of tunable terahertz optical clock," in *Proc. Int. Topical Meeting Microwave Photonics*, Awaji, Japan, 2002.

[15] V. Hietala, G. A. Vawter, T. M. Brennan, and B. E. Hammons, "Traveling-wave photodetectors for high-power, large-bandwidth applications," *IEEE Trans. Microwave Theory Tech.*, vol. 43, pp. 2291–2298, Sept. 1995.

[16] K. S. Giboney, M. J. W. Rodwell, and J. E. Bowers, "Traveling-wave photodetector theory," *IEEE Trans. Microwave Theory Tech.*, vol. 45, pp. 1310–1319, Aug. 1997.

[17] M. Alles, U. Auer, F.-J. Teude, and D. Jäger, "Distributed velocity matched 1.55 $\mu$m InP traveling-wave photodetector for generation of high millimeterwave signal power," in *IEEE MTT-S Dig.*, Baltimore, MD, 1998, pp. 1233–1236.

[18] K. Kato, "Ultrawide-band/high-frequency photodetectors," *IEEE Trans. Microwave Theory. Tech.*, vol. 47, pp. 1265–1281, July 1999.

[19] A. Stöhr, R. Heinzelmann, A. Malcoci, and D. Jäger, "Optical heterodyne millimeter-wave generation using 1.55 $\mu$m traveling-wave photodetectors," *IEEE Microwave Theory Tech.*, vol. 49, pp. 1926–1933, Oct. 2001.

[20] J.-W. Shi and C.-K. Sun, "Design and analysis of long absorption-length traveling-wave photodetectors," *J. Lightwave Technol.*, vol. 18, pp. 2176–2187, Dec. 2000.
[21] D. Jäger, "Slow-wave propagation along variable Schottky-contact microstrip line," *IEEE Trans. Microwave Theory Tech.*, vol. 24, pp. 566–573, Sept. 1976.
[22] Y.-L. Huang and C. K. Sun, "Nonlinear saturation behaviors of high-speed p-i-n photodetectors," *J. Lightwave Technol.*, vol. 18, pp. 203–212, Feb. 2000.
[23] K. J. Williams, R. D. Esman, and M. Dagenais, "Effects of high space-charge fields on the response of microwave photodetectors," *IEEE Photon. Technol. Lett.*, vol. 6, pp. 639–641, June 1994.
[24] K. J. Williams and R. D. Esman, "Design considerations for high-current photodetectors," *J. Lightwave Technol.*, vol. 17, pp. 1443–1454, Aug. 1999.

**Andreas Stöhr** (M'97) received the Dipl.Ing. and Dr. Ing. degrees in electrical engineering from Gerhard-Mercator Universität Duisburg (GMUD), Duisburg, Germany, in 1991 and 1997, respectively.

Since 1995, he has been a Staff Member of the Optoelectronics Department at GMUD. In 1998 and 1999, he joined the Communications Research Laboratory (CRL), Ministry of Posts and Telecommunications, Japan. He has published more than 60 papers in refereed journals and conferences. His current research interests include the design and fabrication of III–V-based microwave photonic devices and their application in microwave or millimeter-wave fiber-optic transmission systems as well as in optical sensors.

Dr. Stöhr is a Member of the IEEE Lasers & Electro-Optics Society (LEOS) and the Microwave Theory and Techniques Society (MTT). He received the 1997 Annual Award from the Duisburger Universitäts Gesellschaft, and he was a Technical Program Committee (TPC) Member of the International Topical Meeting on Microwave Photonics 2002 (MWP'02).

**Andrei Malcoci** received the Dipl.Ing. in electrical engineering from Politehnica-University-Timisooara (UTT), Romania, in 1997 and the Diploma d'Etudes Aprofondies (DEA) from Université de Haute-Alsace (UHA), Mulhouse, France, in 1998, both in automation and industrial computer science.

In 1997 and 1998, he joined the TROP Group, Mulhouse, France for studies and research in the field of neural networks. He has published ten papers in refereed journals and conferences. From 1998 to 2000, he has been active as an IT Engineer on various projects in the industry. In 2000, he joined the Optoelectronics Department at Gerhard-Mercator Universität Duisburg (GMUD), Duisburg, Germany. His current research interests include the design and fabrication technology of III–V-based millimeter-wave photonic devices.

**Andres Sauerwald** was born in Bottrop, Germany, on January 15, 1977. He received the Dipl.Ing. in electrical engineering from University Duisburg-Essen, Duisburg, Germany, in 2003. His thesis focused on the development of 1.55-$\mu$m electroabsorption modulators (EAM) with traveling-wave electrodes for high-bit-rate and high-frequency optical transmission systems.

Currently, he is working as a Researcher with the Department of Optoelectronics at University Duisburg-Essen. He has published two papers in refereed journals and conferences. His research interests include communication systems, terahertz techniques, and optoelectronic devices.

**Iván Cámara Mayorga**, photograph and biography not available at the time of publication.

**Rolf Güsten**, photograph and biography not available at the time of publication.

**Dieter Stefan Jäger** (F'01) received the Diplomphysiker, Dr.rer.nat., and Habilitation degrees in physics, all from the Westfälische Wilhelms-Universität Münster, Germany, in 1969, 1974 and 1980, respectively.

From 1974 to 1990, he was head of a research group at the Institute for Applied Physics, where he became an Associate Professor of Physics in 1985. During 1989–1990, he was a Visiting Professor at the University of Duisburg, Duisburg, Germany. Since 1990, he has been with the Faculty of Electrical Engineering of the University of Duisburg, where he is head of the Department of Optoelectronics. Since 1998, he has also been Dean of the Faculty. He has published more than 200 papers in books, journals, and conferences proceedings, and he is a reviewer for several journals. He is currently engaged in nonlinear phenomena in solid-state devices for MMIC applications as well as nonlinear optics, ultrafast electrooptics, and optical switching in semiconductors for optoelectronic signal processing. His research interests include ultrafast optoelectronics for microwave power generation and transmission, millimeter-wave optical links for broad-band communication technologies, and picosecond electrooptical measuring techniques. He also has activities in the areas of optical neural technology and optoelectronics for medical applications.

Prof. Jäger is Chair of the German IEEE Lasers & Electro-Optics Society (LEOS) chapter as well as Member of the IEEE Microwave Photonics Steering Committee. He is also a Member of the German Physical Society (DPG), the German Vacuum Association (DVG), the German Society of Information Technology (VDE, ITG), and the German Association for Applied Optics (DGaO). He is correspondent of the Union Radio-Scientifique Internationale (URSI). He is an Honorary Professor of the Brasov University/Romania and Consultant Professor of the Huozhong University of Science and Technology, China.